CHAPTER 4

Results and discussions

This chapter discusses the experimental results from the applied research in chapter 3. It consists of:

4.1 Synthesis of Carbon Nanostructures by CVD Method

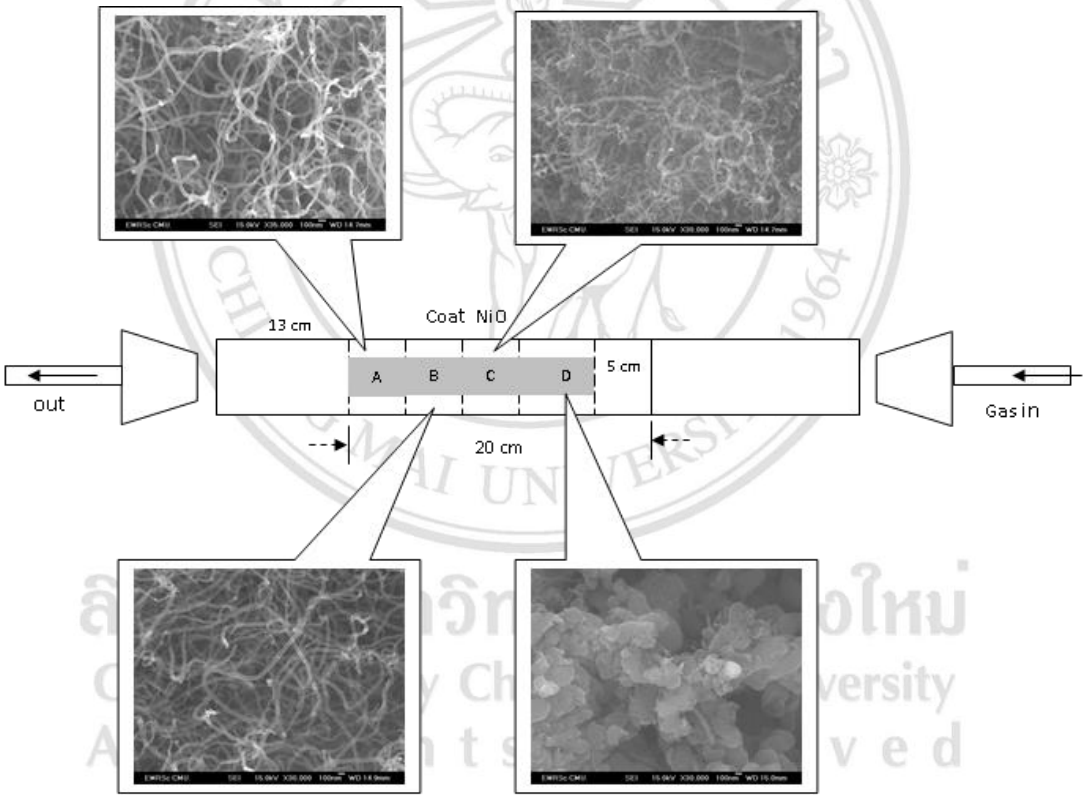

Figure 4.1 Process for synthesis MWNTs by using CVD method

MWNTs was synthesized using the CVD method as shown in Figure 4.1. NiO powder 2.5 grams are used as a catalyst which coated on stainless tube. After that, flow LPG gas at 60 ml/min for 30 min and heated at 425 °C. Finally, heated up the temperature at 675 °C for 9 h. The morphology of MWNTs was confirmed by TEM image as shown in Figure 4.2.

Figure 4.2 TEM image of MWNTs

Ball milling is widely used to reduce the particle size of MWNTs and minimize agglomerated particles. Figure 4.3 (a and b) shows the large MWNT agglomerates that were present after milling with a pestle and mortar.

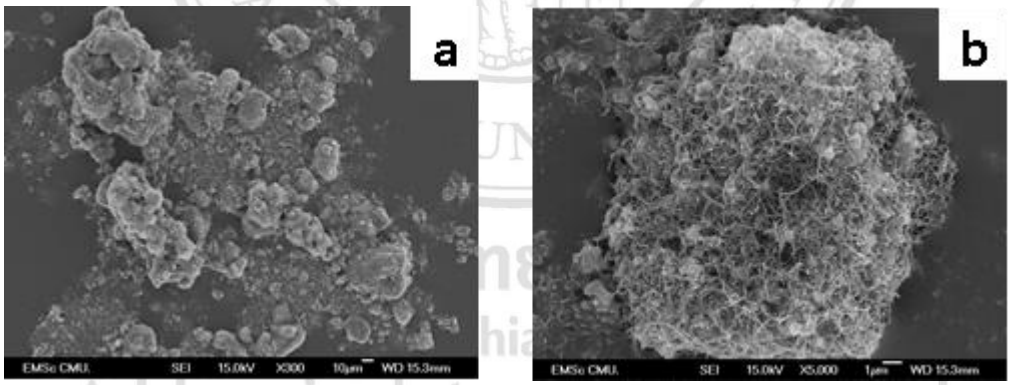

Figure 4.3 MWNTs milled with a mortar and pestle, shown at different magnifications; (a) ×300 and (b) ×5000

Figure 4.4 (a, b, and c) shows SEM images for the samples that were subjected to ball milling for 24, 72 and 120 h, respectively. The size of the agglomerated MWNT decreased with increasing of milling time. This result corresponded Lemine, et al. [1] and Traiphol [2], reporting that increasing ball milling time reduced the size of powder particles. The samples milled for 24 h (shown in Figure 4.4 a) showed MWNTs

aggregate with a wide range of sizes, from small to large (~ 4-20 μm). The MWNT aggregate size was reduced to 3-10 μm in the sample milled for 72 h. The MWNT aggregates had a small size in the sample milled for 120 h (~ 2-5 μm), and the aggregate sizes were relatively homogeneous.

Ammonium polyacrylate (Dispex A40) was ionized in the aqueous medium, and produced NH_4^+ cations, together with polyanions [3]. These ions were adsorbed irreversibly (into or onto) to the MWNT surfaces, causing the MWNTs to become negatively charged.

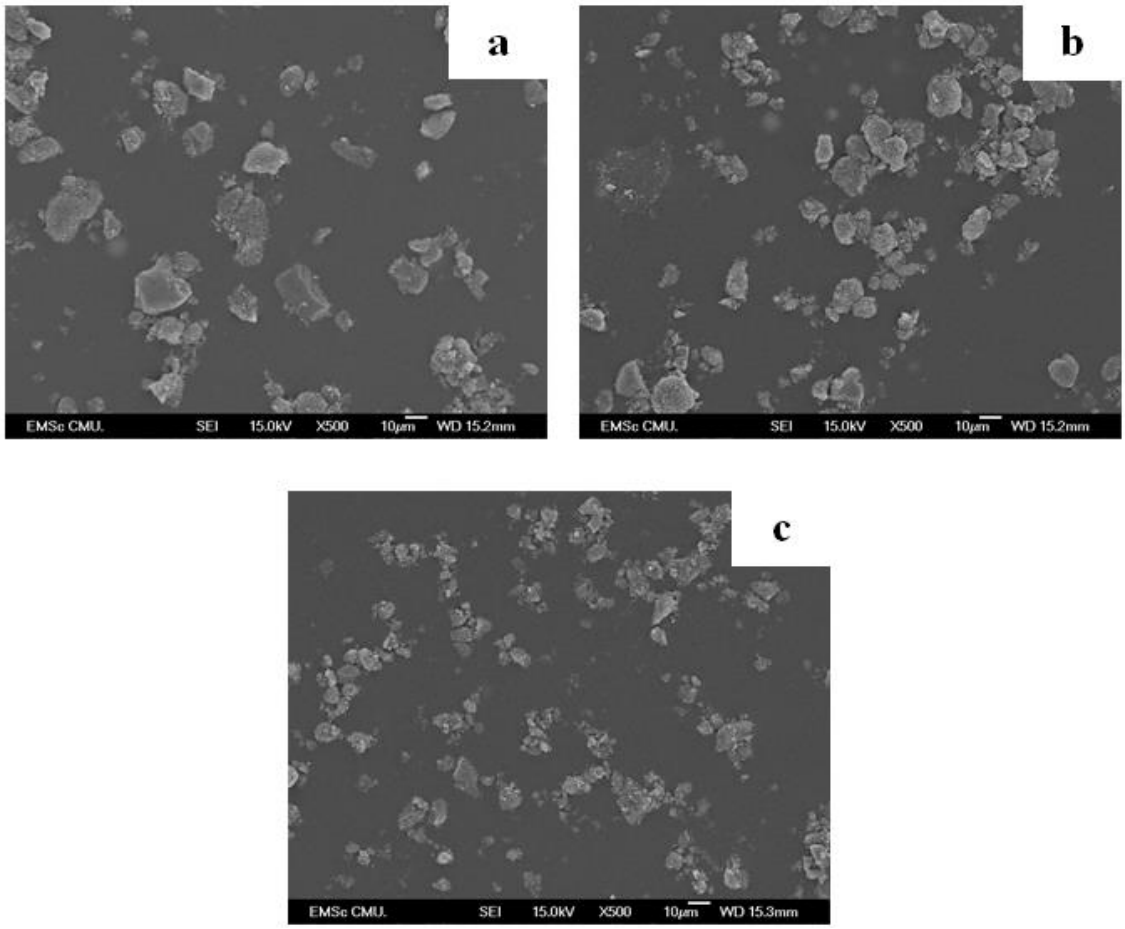

Figure 4.4 SEM images of MWNT solutions with Dispex A40 (a) milled 24 h, (b) milled 72 h, (c) milled 120 h at × 500 magnifications

The discrepancy and the sizes measured using the different pores can be understood by considering the resolution of detection of the two pores. The bigger pore had a lower detection limit of ~2.2 μm, so any particles smaller than this were lost in the noise, and

were not detected. Using the smaller pore, particles as small as ~1 μm and at least as large as ~4 μm could be detected; this range included the aggregates detected using the bigger pore, so the obvious question is to ask why were the mean measured sizes different for the different pores? The answer is that the concentration of the smaller, sub ~2 μm particles was much higher than that of the larger particles. A concentration analysis (data not shown here) showed that the concentration of particles with sizes from 2.4 μm to 4 μm was of the same order of magnitude for both pores, so the distribution peak for the larger particles is in fact replicated (but on a much smaller scale) in the data for the smaller particles.

These results are good agreement with the results from SEM, and confirms the ability of this technique to measure very polydisperse samples. The results showing a trend of reducing size for the larger aggregates but not for the smaller particles makes intuitive sense, because it is likely that the larger aggregates were broken down by the ball milling more readily than the smaller aggregates, which probably remained in the gaps between the balls.

4.2 Melt-mixing the composite materials, and properties measurements

It is well known that increase in temperature result in decrease in the specific surface energy [4] of polymers, which in turn results in shrinkage and compaction of the polymer. A mechanism that describes this process using a densification coefficient was suggested by the Scherer and Garino models [5]. The coefficient depends on the bulk density and specific surface energy of the compact polymer. In other words, the reduction of the specific surface energy that occurs with increases in the temperature causes the air inside the open pores to be removed from the compact polymer, and the pores are thus closed. This model describes the behavior well until the closed pores form, which occurs at $\rho/\rho_s = 0.942$, where ρ is the polymer density and ρ_s is the full density of the polymer. After the pores are closed, the viscosity of the polymer melts decreases as the temperature increases. Because the viscosity of the polymer melts decreases, the polymer chains in the melt become shorter [6], which means that the diffusion of air through the polymer melts becomes easier. In addition, the pressure of the hot air inside the bubbles increases, causing the diffusion rate of the air to increase [7], as suggested by the diffusion model.

Under one-step heating, the porosity of the sample increased when the amount of MWNTs in the MWNT-LLDPE composite was increased, as shown in Figure 4.5a and Scheme 4.1a.

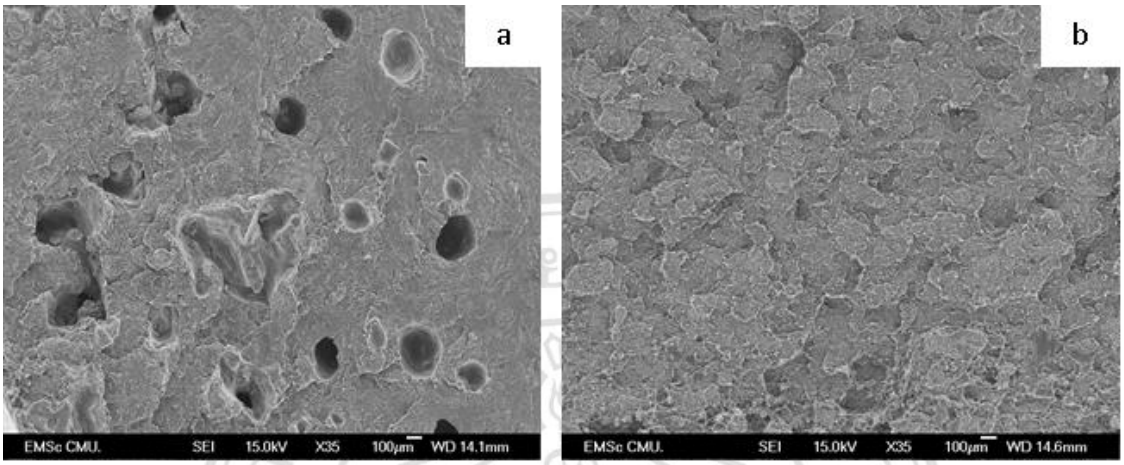

Figure 4.5 SEM images of (a) sample prepared using single-step heating, and (b) sample prepared using four-step heating at 5 vol.% MWNT

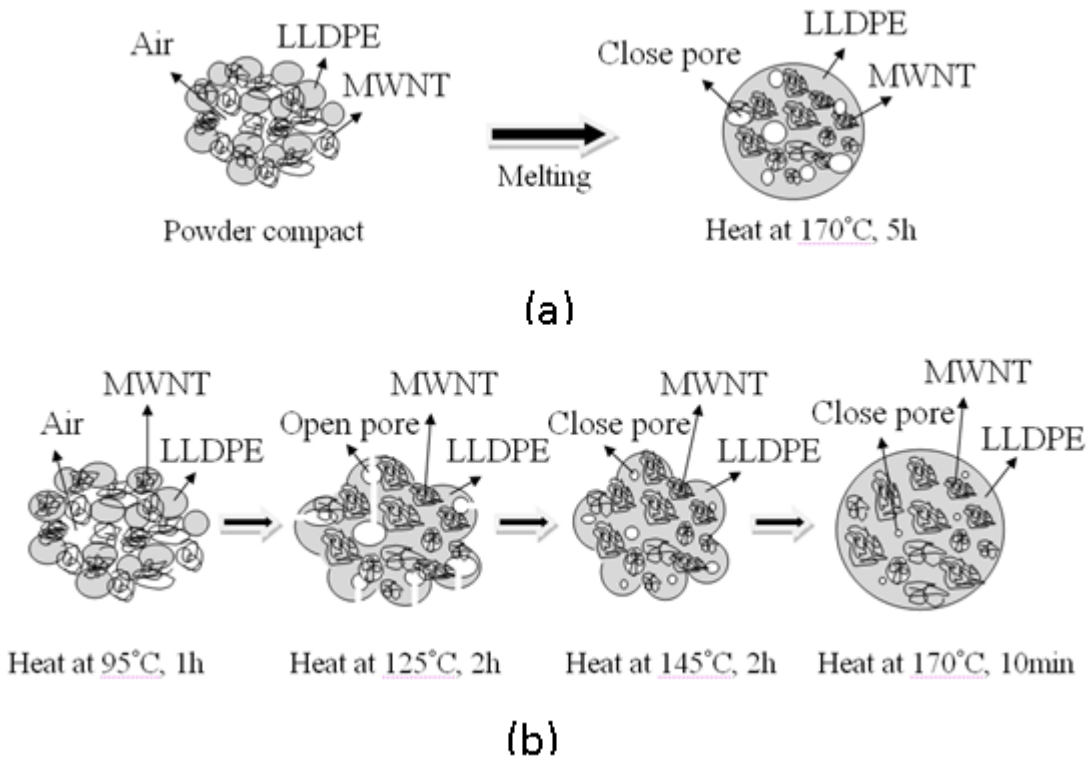

Scheme 4.1 Diagrams of (a) single-step heating and (b) four-step heating for MWNT-LLDPE melt mixing

In addition, the effects of temperature gradient caused the early surface melting of the powder compact; this was because of the high concentration of air inside the polymer melts when the powder compact was heated from room temperature to 170 °C. Therefore, for prepared samples with the same density, the holding time of the one-step heating greater than for the four-step heating. Under four-step heating, the moisture was eliminated as the temperature was increased from room temperature to 95 ºC over a period of 1 h. To melt the LLDPE and thus to remove the air inside the open pores to form closed pores the temperature was then raised to 125 ºC over a period of 2 h, as described by the Scherer and Scherer and Garino models. To ensure the complete melting of the LLDPE and the removal of the air inside the bubbles in the polymer melts, the temperature was then raised to 145 ºC over a period of 2 h, as shown in Figure 4.5b and Scheme 4.1b. To allow the polymer enough time to form a highly crystalline structure, the sample was heated to 170 ºC over a period of 10 min before the sample was allowed to cool naturally [8, 9].

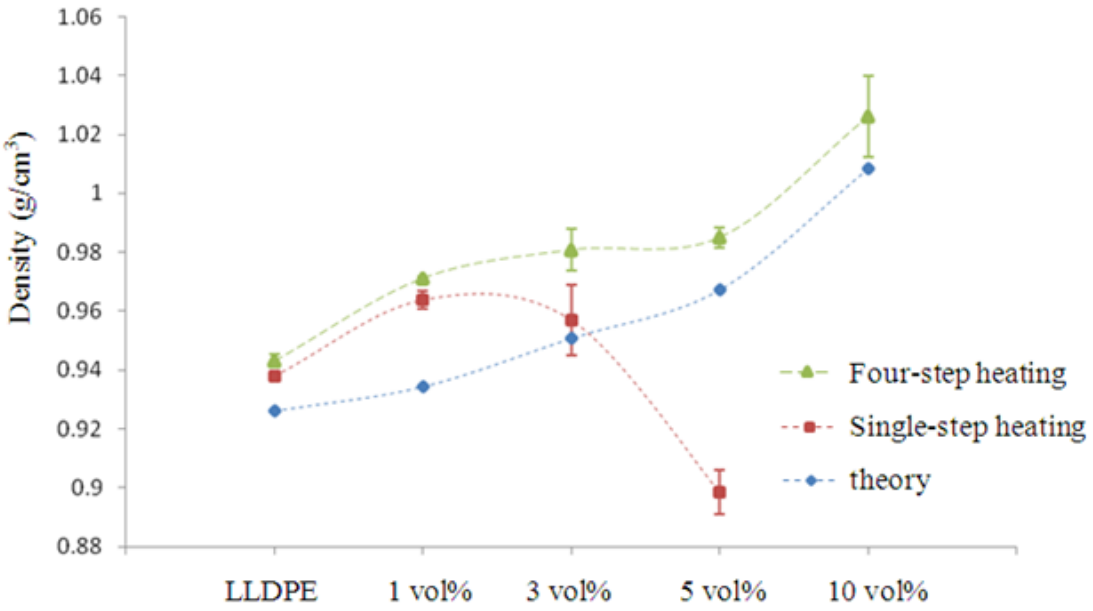

Figure 4.6 Density of samples prepared using four-step heating, single-step heating, shown with the theoretically predicted density

Figure 4.6 shows that the density of the samples prepared using single- and four-step heating was higher than the theoretical values for the density of pure LLDPE with 1 vol.% or 3 vol.% MWNTs. This resulted from the effects of the degree of crystallinity in the LLDPE, as determined in the XRD characterization (Figure 4.7). The degree of

crystallinity in LLDPE powder, and LLDPE prepared used single- and four-step heating was calculated using Hemans and Weidinger's method [8, 10]; the calculated values were 40.28%, 47.26%, and 49.47%, respectively. This effect resulted in density values for the composite materials that were higher than the theoretical values. The single-step heating samples with 3 and 5 vol.% MWNTs had low density, because of the effects of the porosity (Figure 4.5). The 10 vol.% MWNT single-step heating sample could not be analyzed; because of the high porosity, it could not be pulled out of the mold.

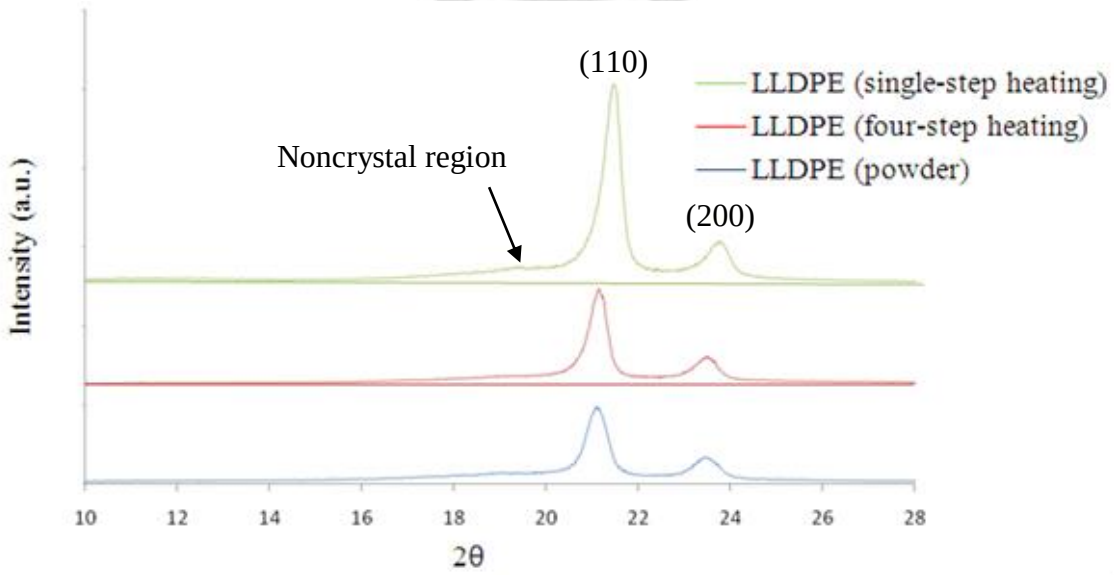

Figure 4.7 XRD peaks for the LLDPE powder, four-step heating LLDPE, and single-step heating LLDPE samples

The mechanical properties of the LLDPE/MWNT composites were investigated using a tensile testing machine and impact strength tests (charpy). The results are shown in Figures 4.8-4.11.

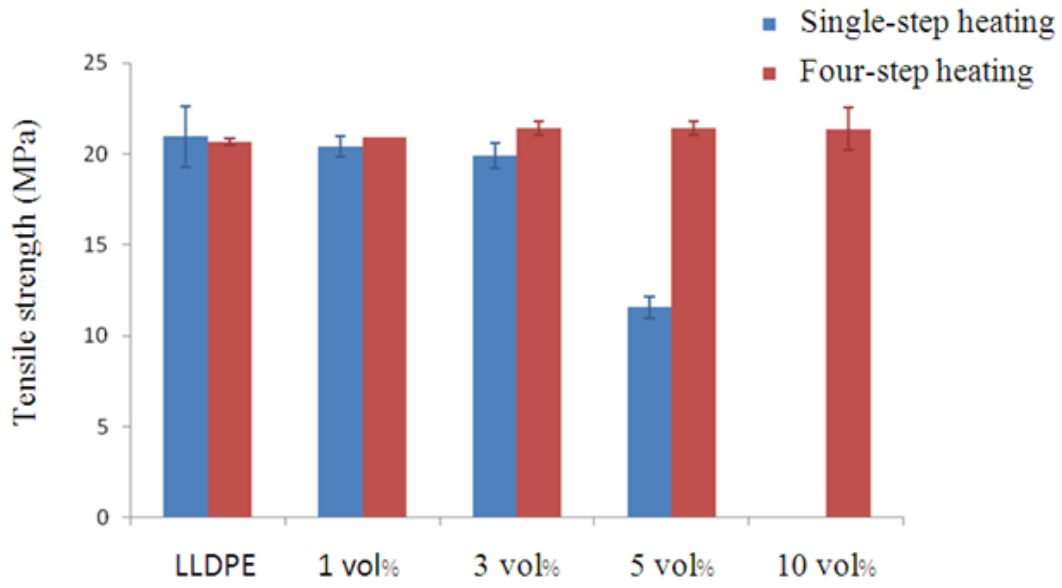

Figure 4.8 Tensile strength of samples prepared using single-step heating and four-step heating

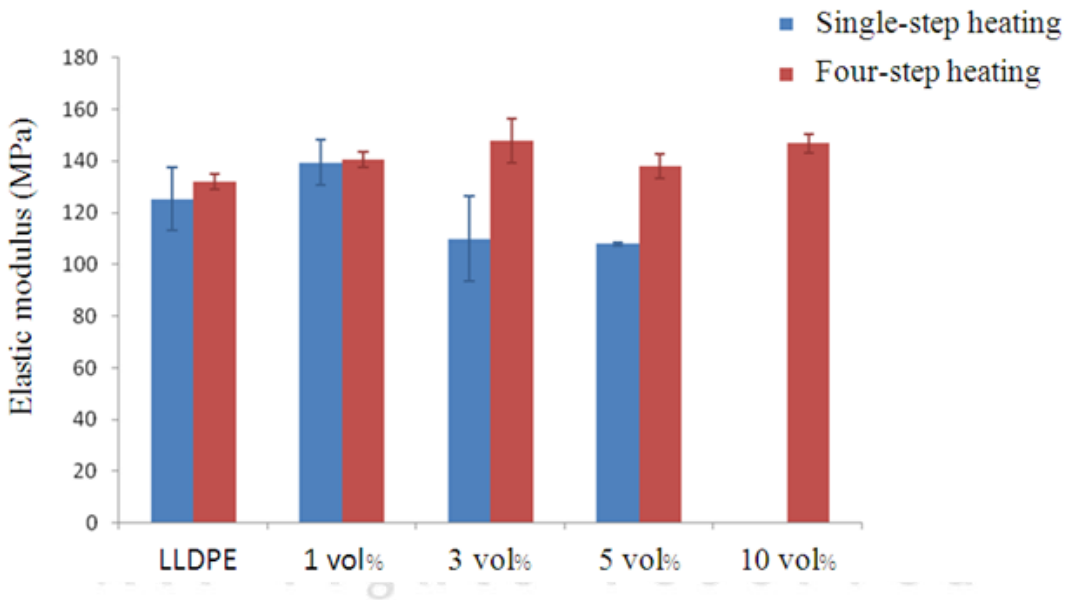

Figure 4.9 Elastic modulus of samples prepared using single-step heating and four-step heating

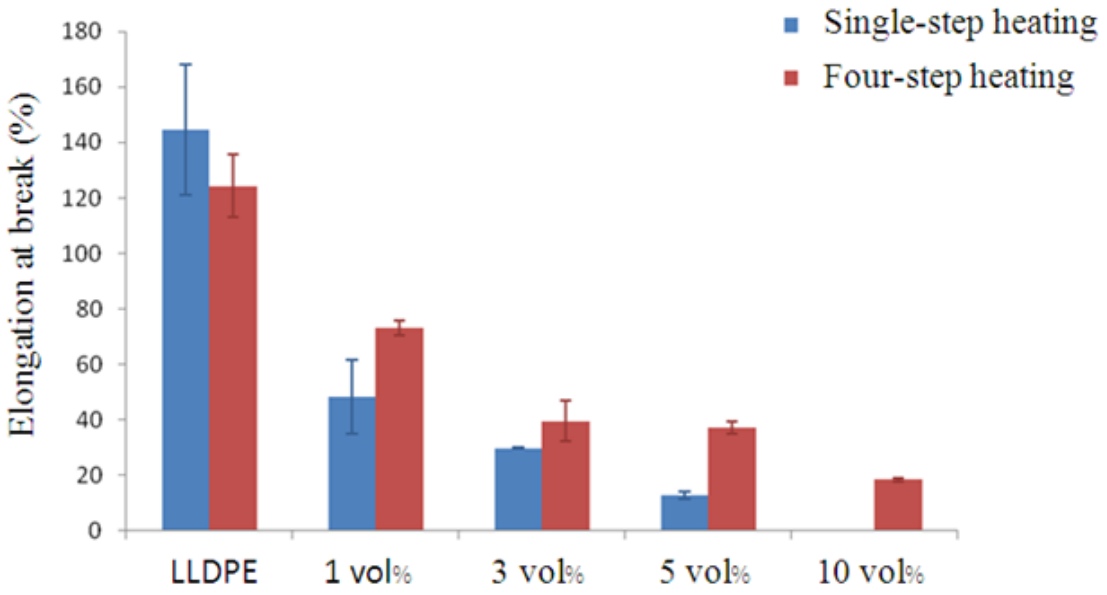

Figure 4.10 Elongation of samples prepared using single-step heating and four-step heating

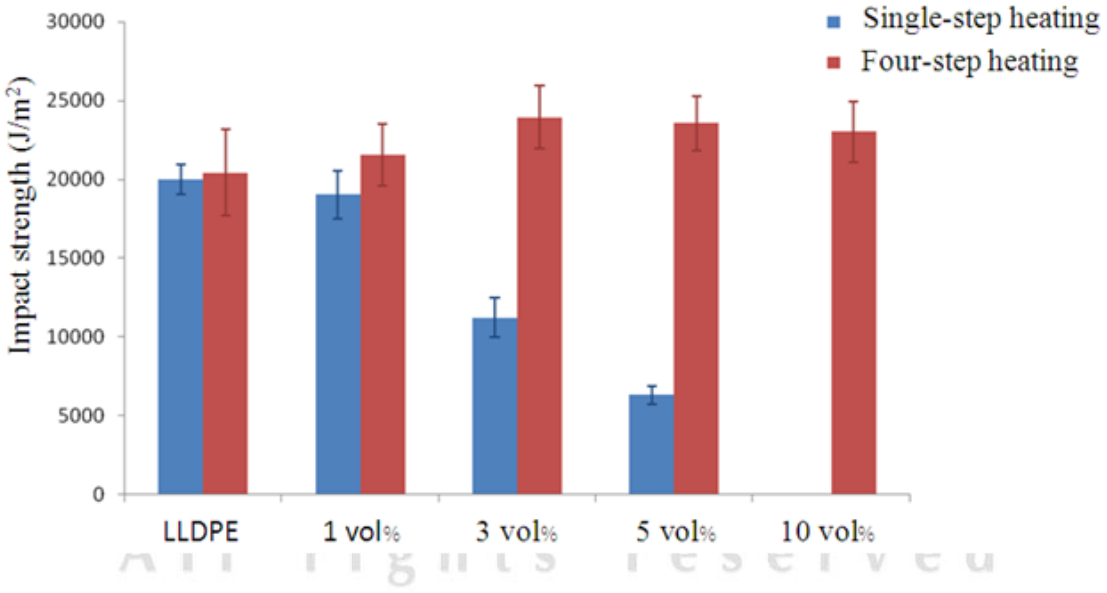

Figure 4.11 Impact strength of samples prepared using single-step heating and four-step heating

As shown in Figure 4.8, the tensile strength decreased with the increased volume fraction of MWNTs in the 1, 3 and 5 vol.% (20.42, 19.90, and 11.58 MPa, respectively) in samples prepared using single-step heating. The elastic modulus results were similar for the single-step heating samples. The elastic modulus values for the MWNT 1, 3 and 5 vol.% samples were 139.46, 109.90, and 107.94 MPa respectively. For the

LLDPE/MWNT composite samples prepared using four-step heating, the tensile strength and elastic modulus values tended to increase with the increasing volume fraction of MWNTs. The tensile strength values were 20.91, 21.40, 21.41, and 21.39 MPa for the 1, 3, 5 and 10 vol.% MWNT samples, respectively. These values were similar to those found by Lee et al. [7]. They studied the mechanical properties of LLDPE/CNF composites with three different concentrations of CNF (varying the content of CNF from 0-15 wt.%). The tensile strength values were approximately 20 MPa.

Kuan et al. [9] investigated the tensile strength of LLDPE/MWNT composites prepared using a water – crosslinking reaction, and varied the MWNT concentration from 0 to 4 phr (parts per hundred parts of polymer resin); the tensile strength values ranged from 19.0 to 21.7 MPa. The elastic modulus values (Figure 4.9) for the sample using MWNT concentrations of 1, 3, 5 and 10 vol.% were 140.68 MPa, 147.87 MPa, 138.03 MPa, and 146.81 MPa, respectively. These results occurred because the defect porosity in the single-step heating samples (Figure 4.5) produced decreases in the tensile strength and elastic modulus when the MWNT volume fraction was increased in the composite materials. When four-step heating was used to melt the composite materials, this effect disappeared. Figure 4.10 shows elongation at break values for the samples prepared using single- and four-step heating. The elongation at break values tended to decrease with increasing volume fraction of MWNTs, because the effects of the degree of crystallinity in the LLDPE increased (Figure 4.7) [8]. The porosity in the single-step heating also contributed to the decreases in the elongation at break values (the elongation at break values for the samples prepared using single-step heating were lower than those for the four-step heating samples).

The results from the impact strength tests on the samples prepared using single- and four-step heating are shown in Figure 4.11. The porosity in the samples prepared using single-step heating resulted in decreases in the impact strength values as the MWNT volume fraction was increased (the 1, 3, and 5 vol.% MWNT samples had values of 19041 J/m^2, 11239 J/m^2, and 6315 J/m^2, respectively. The four-step heating samples showed increasing impact strength values with increases in the volume fraction of MWNTs. The 3 vol.% MWNT composite showed the maximum impact strength value

(23947 J/m^2). The four-step heating samples of 3 vol.% MWNT composite have optimum mechanical properties that can improve tensile strength, elastic modulus and impact strength up to 3.53%, 12.04% and 19.67%, respectively relative with pure LLDPE.

4.3 MWNTs/polymer composites coated on copper and aluminum sheet

MWNTs at 1, 3, and 5 vol.% were mixed with LLDPE powders and were then ball milled for 5 h. Films of the mixing powder were then prepared by the hot press method at a pressure of 5 bars and a temperature of 180 ºC for 15 min. For the adhesive bonding layer, MWNTs at 10, 20, 30 and 40 vol.% were mixed with PVB in ethanol and stirred at room temperature for 24 h. MWNTs/PVB films were then prepared by a spin coating technique at 3000 rpm on to the copper and aluminum sheet which was prepared according to ASTM D2651-01 (shown in Figure 4.12–4.13). Flow charts of the over all process are shown in Figure 3.2.

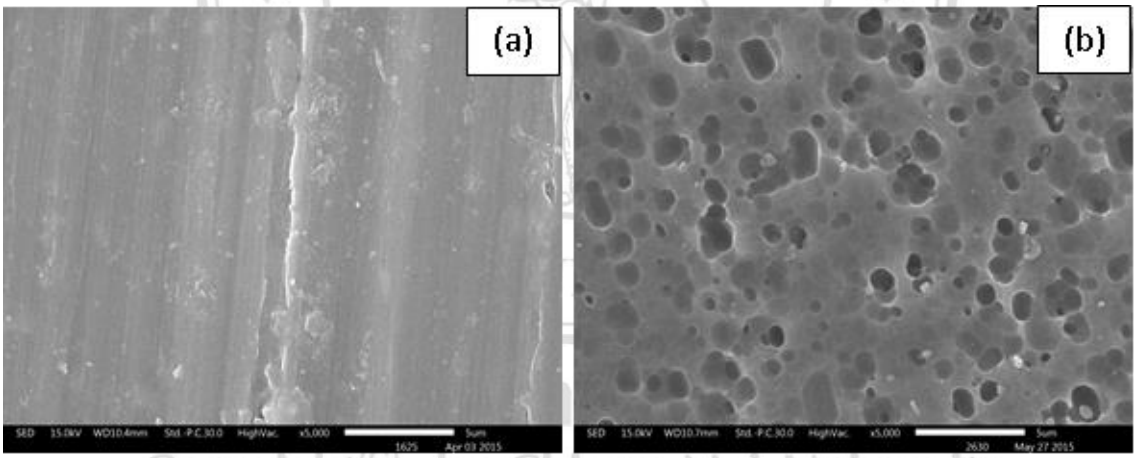

Figure 4.12 Surface of Al plate (a) before and (b) after chemical treatment

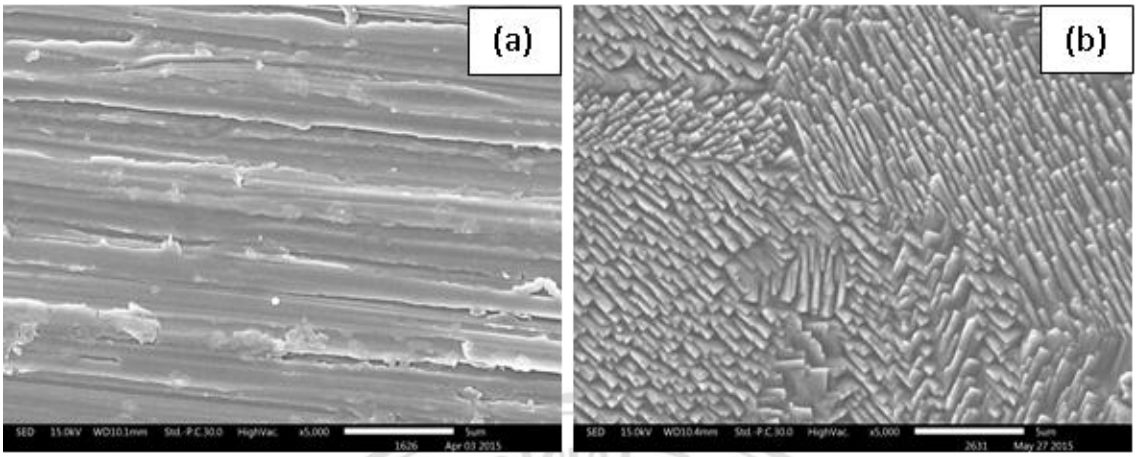

Figure 4.13 Surface of Cu plate (a) before and (b) after chemical treatment

The thickness of MWNTs/PVB sheet has about 4 µm and distribution of MWNTs was observed by SEM in BED mode. It can be clearly seen that MWNTs are well dispersed in PVB sheet. Solar transmission (UV, IR, and VL) of PVB sheet and MWNT/PVB composite at 10, 20, 30, and 40 vol.% of MWNTs. The value of solar transmission was decreased when increasing MWNTs.

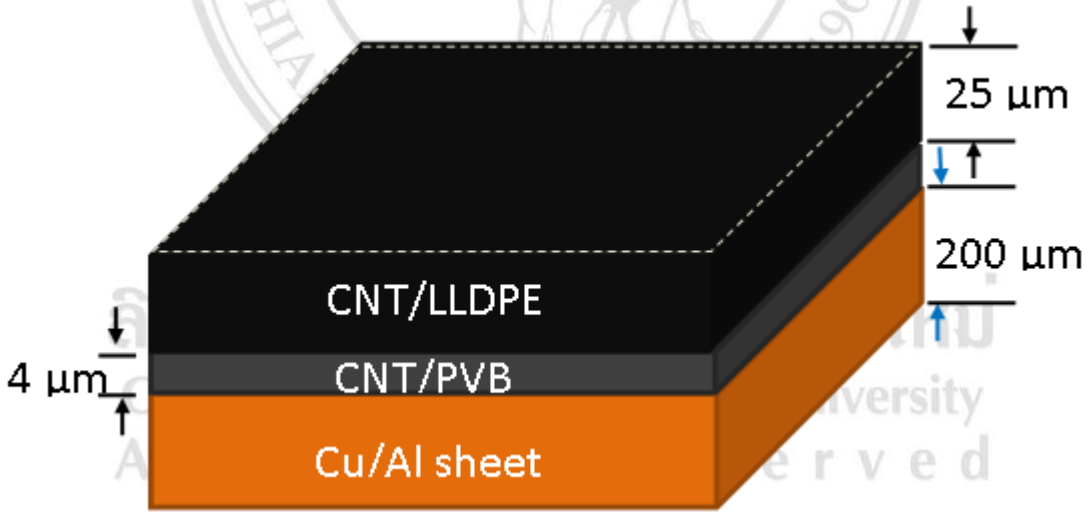

Scheme 4.2 Diagram for preparation MWNTs/polymer composites coated on copper and aluminum sheet

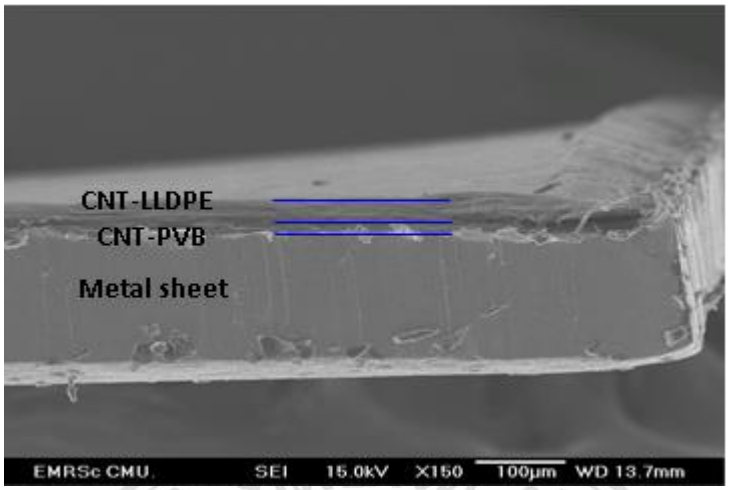

Figure 4.14 SEM image of MWNTs/polymer composite on metal sheet

Scheme 4.2 shows a diagram for the preparation of MWNTs/polymer composites coated on copper and aluminium sheets. MWNTs/LLDPE coated on copper and aluminium sheet at 180 °C for 15 min and used the 5 bar of pressure and MWNTs/PVB composite was used for the bonding layer between MWNTs/LLDPE and the metal sheet (copper or aluminium). The thickness of MWNTs/polymer composite was about 30 µm and was observed by SEM as shown in Figure 4.14.

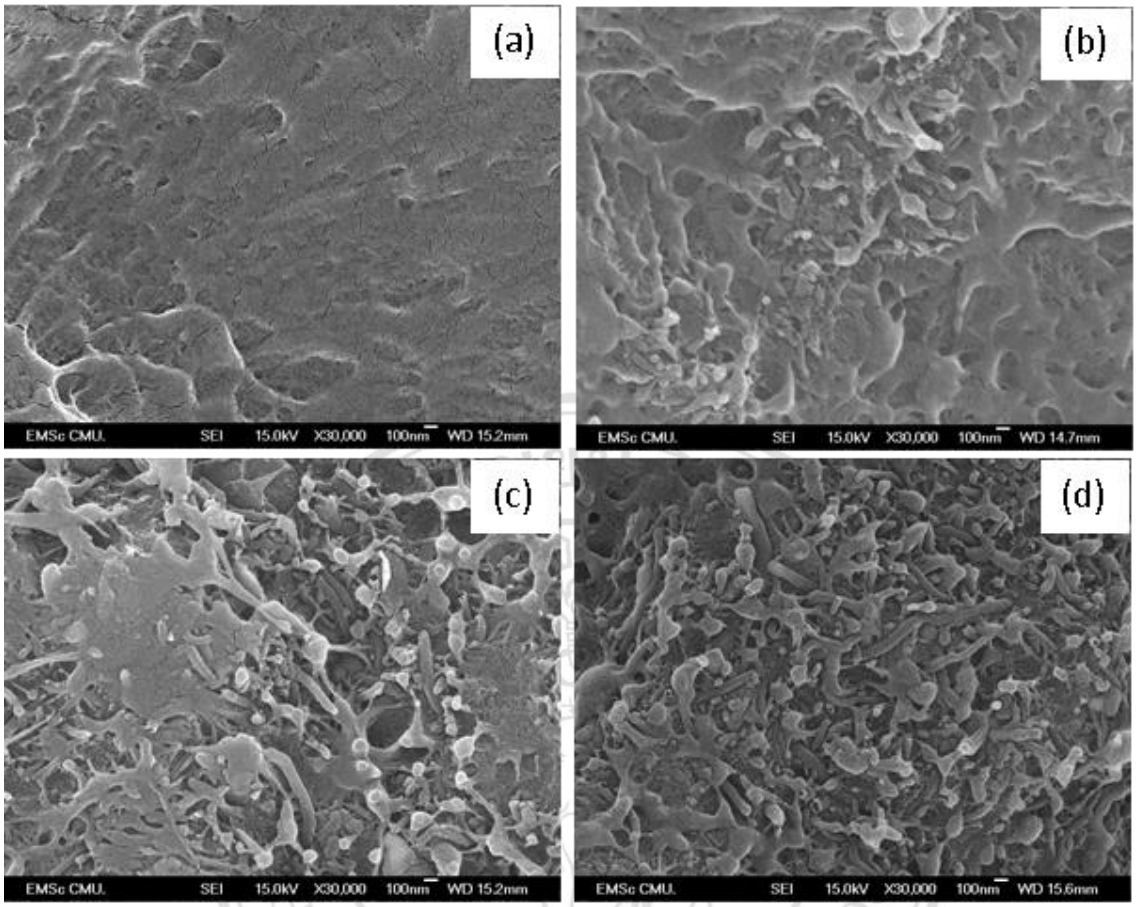

Figure 4.15 SEM images of MWNTs/LLDPE composites prepared with (a) 0 vol.%, (b) 1 vol.%, (c) 3 vol.%, and (d) 5 vol.% of MWNTs.

The microstructures of the MWNTs/LLDPE films prepared with various volume fractions of MWNTs were observed by SEM as shown in Figure 4.15 (a-d). It can be seen in Figure 4.15a that the morphology of the pure LLDPE film was consistent with that of a normal LLDPE image [11]. It is noted that the MWNTs were randomly distributed into the LLDPE matrix as shown in Figure 4.15b–d with volume fraction of 1, 3, and 5 vol.%, respectively. MWNTs in the LLDPE matrix were evenly spread along the surface and maximized their covered fraction at 5 vol.%, as shown in Figure 4.15 (d).

4.4 Mechanical property of adhesive bonding

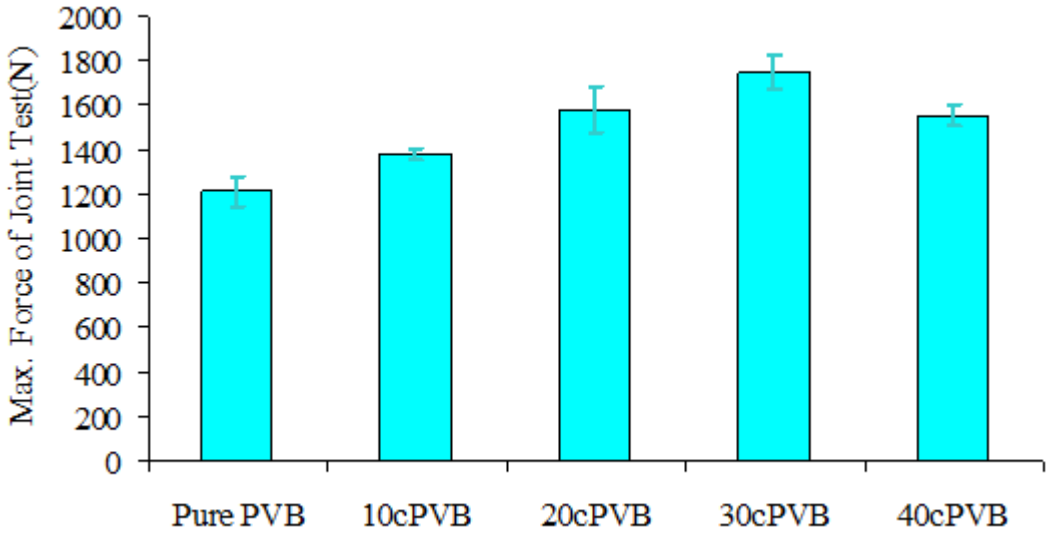

Figure 4.16 Joint test results of pure PVB, 10, 20, 30, and 40 vol.% MWNTs/PVB composites coated on Cu sheets

The maximum shear forces, for the joint test of pure PVB, 10, 20, 30, and 40 vol.% MWNTs/PVB composite coated copper and aluminium sheets, are shown in Figure 4.16 and Figure 4.17, respectively. It is well known that the maximum force applied to the joint test increased with the increasing of the volume fraction of MWNTs. However, at 30 vol.% of MWNTs, the maximum shear strength was achieved (approximately 1800 N and 4500 N for coated copper and aluminium sheets, respectively). It was anticipated that the effect of an agglomeration between the tubes at 40 vol.% of MWNTs started to weaken the composite strength. Moreover, the effect of surface metal after treatment can increase polymer/metal interface bonding, as follows in chapter 2 section 5.1. In figure 4.12 and 4.13, aluminium plate shows a pitted surface and copper plate shows a pattern of horizontal furrows arrayed at different angles that also improves the bond of polymer to sheet.

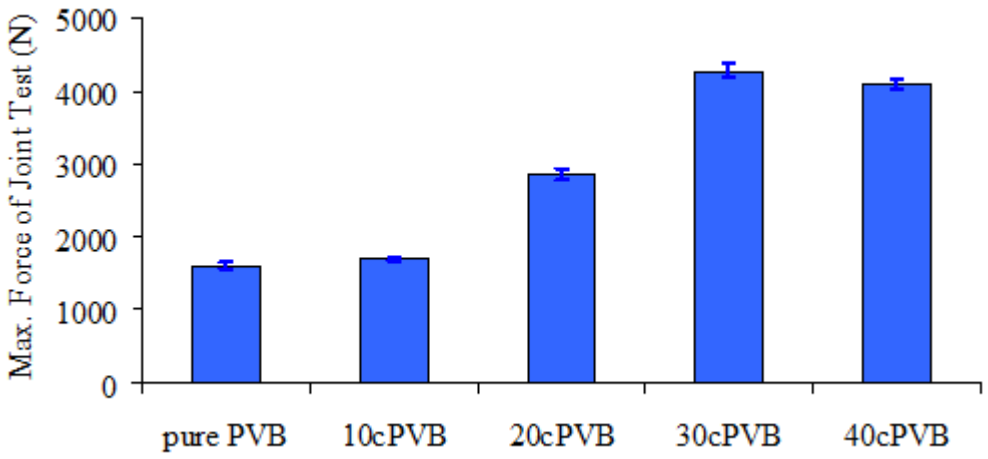

Figure 4.17 Joint test results of pure PVB, 10, 20, 30, and 40 vol.% MWNTs/PVB composites coated on Al sheets

4.5 Heat absorb of the MWNTs/LLDPE composite coated on Cu sheet

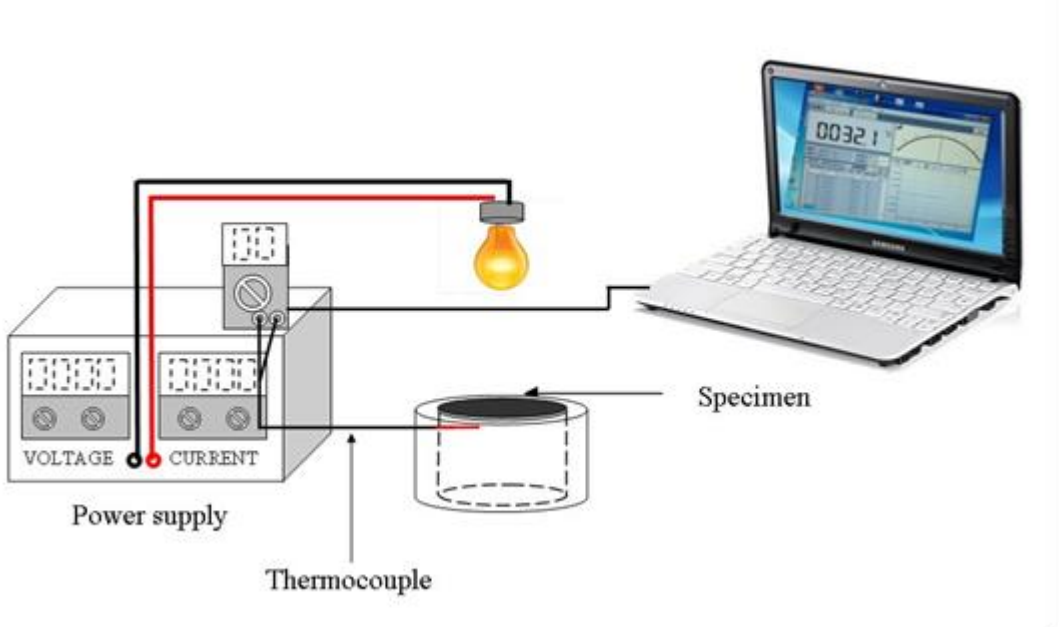

Scheme 4.3 Diagram of heat absorbing test

The heat absorption test for MWNTs/LLDPE composite coated on to copper and aluminium sheet using the MWNTs/PVB composite for the bonding layer measure is shown in Scheme 4.3. The specimen for testing heat absorption used MWNTs/PVB sheet at the same thickness (~ 4 μm) for 10, 20, 30, and 40 vol.% of MWNTs/PVB composite for the bonding layer with the distance between the specimen and light source at 15 cm. The results from these tests are shown in Figure 4.18 and 4.19.

Figures 4.18 and 4.19 show the temperature absorption from the light source for the 5 vol.% sample of MWNTs/LLDPE composite, using 10, 20, 30, and 40 vol.% MWNTs/PVB composite at a thickness of 4 µm for the bonding layer coated onto the copper and aluminium sheets that were black spray coated and positioned at a distance of 15 cm from the light source to the specimen. The specimen with 5 vol.% MWNTs/LLDPE using 40 vol.% MWNTs/PVB composite for bonding layer coated to copper sheet has a higher temperature absorption rate than the other lower percentages of MWNTs/PVB (~ 43 °C).

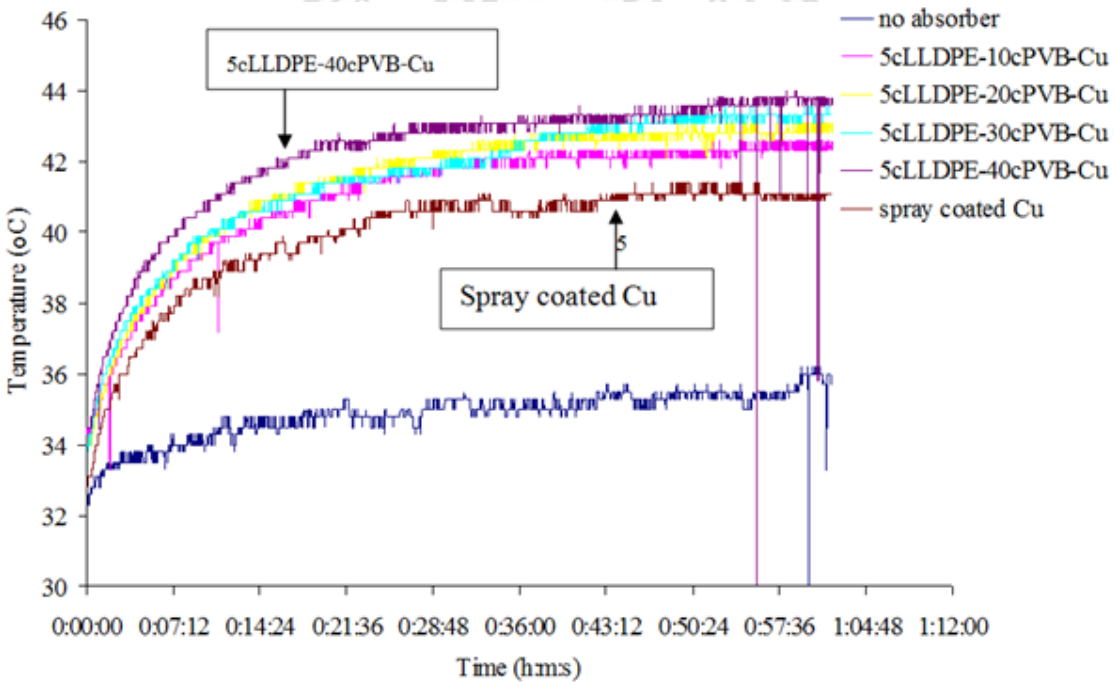

Figure 4.18 Heat absorption of the sample 5cLLDPE/(10–40) vol.% MWNTs/PVB composites coated on Cu sheet, with the distance between light source and specimen at 15 cm

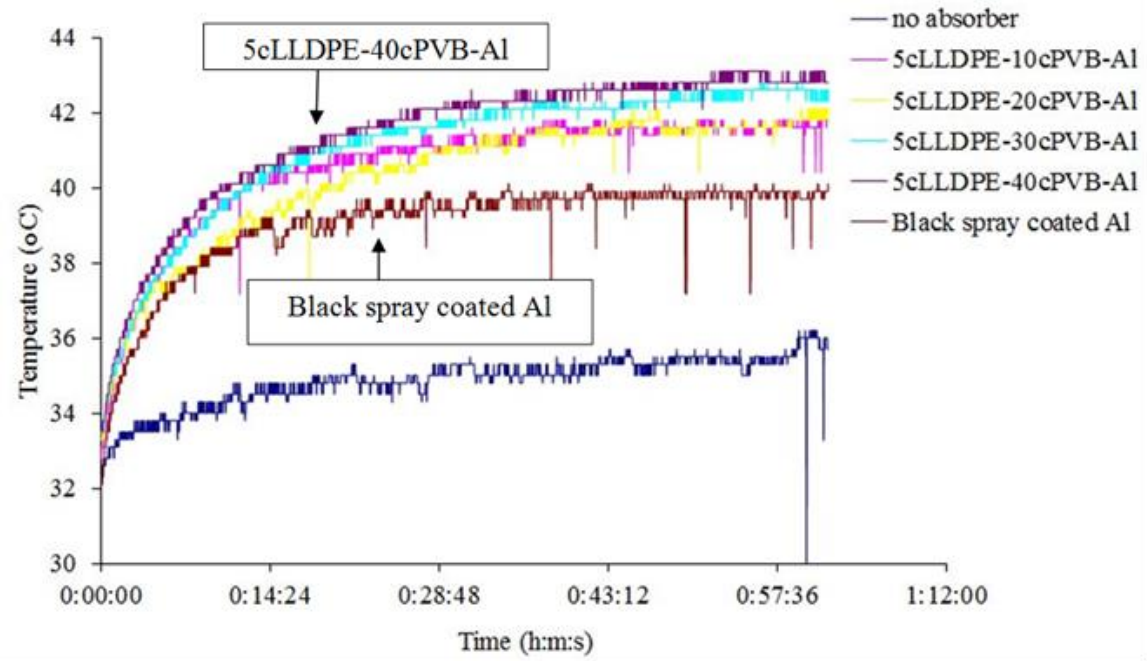

Figure 4.19 Heat absorption of the sample 5cLLDPE/(10–40) vol.% MWNTs/PVB composites coated on Al sheet with the distance between light source and specimen at 15 cm

4.6 The reflectance spectra of MWNTs/LLDPE composites

Figure 4.20 shows the spectral reflectance with four different volume fractions of MWNTs/LLDPE. The UV-Vis absorbance of the MWNTs/LLDPE composites was evaluated from UV-Vis reflectance spectra using the equation; $\alpha+R+T=1$, where α is absorptance, R is reflectance, and T is transmittance. When the MWNTs/LLDPE was coated onto the copper sheet, the transmittance is about zero due to the copper sheet being opaque and therefore the absorptance is $\alpha=1-R$. The absorptance increased with the increasing the volume fraction of MWNTs reaching a maximum of 0.95 at 5 vol.% MWNTs/LLDPE.

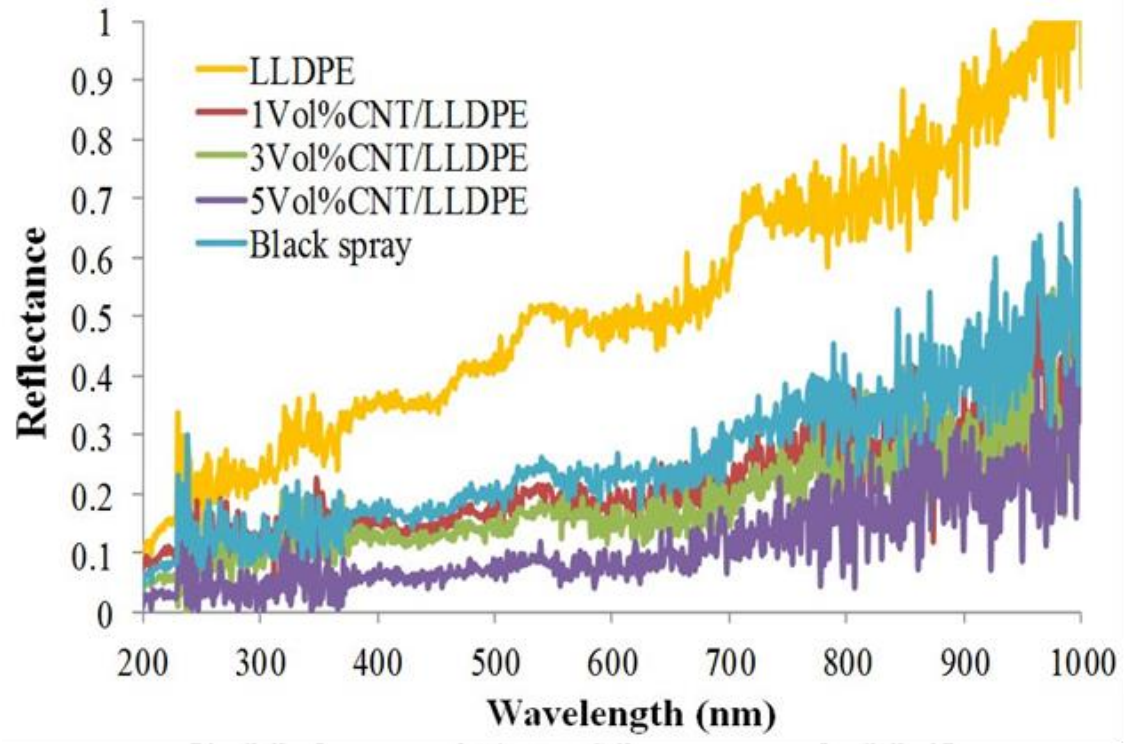

Figure 4.20 The reflectance spectra of MWNTs/LLDPE composites at 0, 1, 3, and 5 vol.% of MWNTs and black color spray on Cu sheets

Comparisons of solar absorptance by this technique and by others are summarized in Table 4.1. As discussed above, the solar absorption depends on the thickness, the density, the surface roughness, and the volume fraction of the black fillers in the matrix. However, Roro et al. [12], Chen and Bostrom [13] reported that MWNT coated aluminum substrates showed the absorptions of 0.84 and 0.79–0.90, respectively. The low absorption of these coatings was probably due to the low thickness and density of the films. In contrast with Cheng et al., [14] Bera et al., [15] and Feng et al. [16] reported high absorptance of 0.949, 0.975, and 0.95, respectively. The high absorptions of these coatings were probably due to the high thickness and high surface roughness, as well as the dispersion of the black base evenly through the matrix. For this work, the results of the coatings achieved the solar absorption of 0.95. The high absorption of these coatings was due to the high surface roughness and the better distribution of MWNTs in LLDPE as shown in Figure 4.15 (d).

Table 4.1 Comparison of solar absorptance at various absorbed materials and coating methods.

Result from	Solar absorptance (α)	Substrates	Absorbed materials	Coating methods
Cheng, et al. [14]	0.949	Copper	carbon-titania nanocomposite films	polymer-assisted photopolymerization-induced phase-separation
Bera, et al. [15]	0.975	Aluminum	CNT-based black coatings	solution-processed spray
Feng, et al. [16]	0.95	stainless steel	TiN/TiSiN/SiN	dc reactive magnetron sputtering.
Roro, et al. [12]	0.84	Aluminum	MWNTs/NiO nanocomposites	sol-gel.
Chen and Bostrom [13]	0.79–0.90	Aluminum	CNTs	electrophoretic
This work	0.95	Copper	MWNTs/LLDPE	hot press.

4.7 Heat absorbed by water from solar radiation

Heat absorbed by water from solar radiation was determined by using a home-made method. This consisted of the solar radiation from the sun (in a clear-sky day from 11:00 to 13:00 o'clock in April at Chiang Mai, Thailand) and a glass box $12\times12\times6$ cm^3 in size, as schematically shown in Scheme 3.3 in chapter 3. When converting the value of water heat absorbed for the energy per area of the sample, the following equation was used, $Q = mc(T_{out}–T_{in})$ where Q is the solar energy collected, c is the specific heat of the water, m is the mass of water flow rate in (kg/s) as shown in figure 4.21.

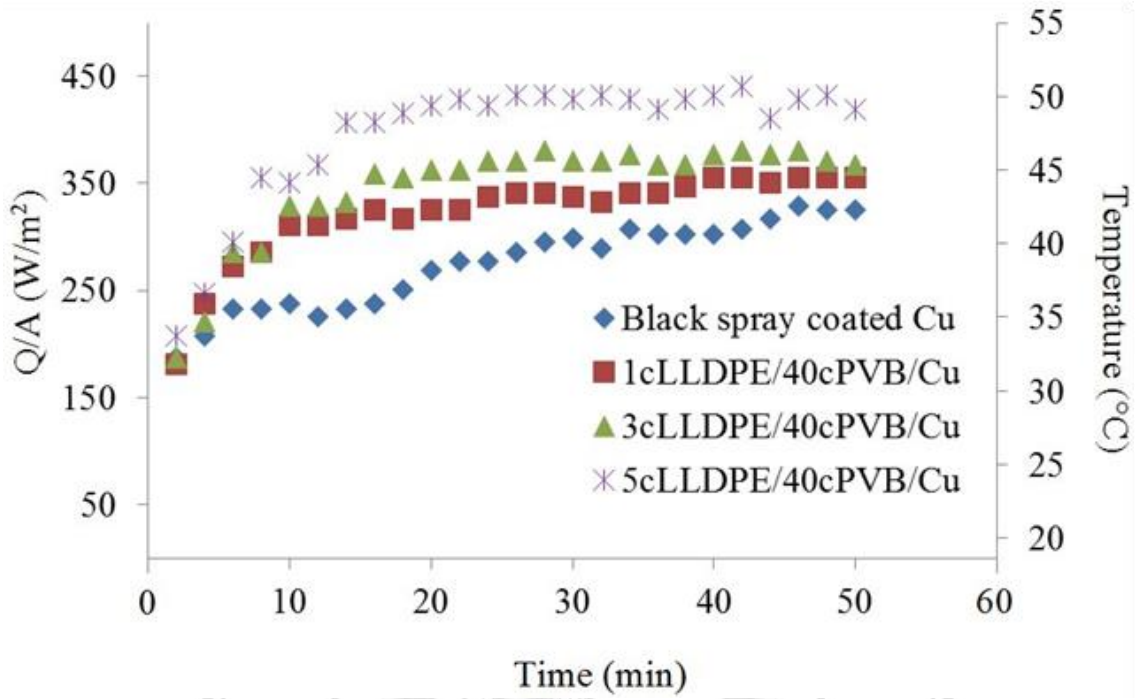

Figure 4.21 Energy and temperature of the water absorbed heat versus the testing time of 1, 3, and 5 vol.% MWNT/LLDPE composites sprayed black

The solar water heaters were tested for the absorbed solar radiation through the black paint and the 1, 3, and 5 vol.% MWNT/LLDPE composites with the 40 vol.% MWNT/PVB composites for the bonding layer coated on the copper sheets. The results of the sample using 5 vol.% MWNT/LLDPE composites showed a maximum temperature of 52 °C. To convert the absorbed heat of water to the energy per unit area of the samples, the following equation is expressed:

$$P = dQ/dt = (dm/dt)\, c_w\, (T_{out} - T_{in}) \qquad (4.1)$$

Where P is the power, Q is the collected solar energy, c_w is the specific heat of the water, dm/dt is the mass flow rate of water. The absorbed solar power was calculated by Q over the time and the area of the solar absorber (A = 0.007854 m^2). The maximum energy absorption per unit area was found in the sample using 5 vol.% MWNT/LLDPE composites with approximately 450 W/m^2, as shown in figure 4.21. In other words, the energy conversion efficiency was approximately 40%.

In Figure 4.21, thermal conductivity of the samples was calculated by Fourier's law and compare with the rule of mixture model and the series model (as shown in Table 4.2).

Table 4.2 Thermal conductivity of MWNTs/LLDPE composite

% Volume		Thermal conductivity k_C (W/m°C)		
MWNTs	LLDPE	(rule of mixture)	(series model)	(Fourier's law)
1	99	30.32	0.32	2.40
3	97	90.31	0.33	2.48
5	95	150.30	0.34	2.59
Black spray	-	-	-	2.39

Many methods can be used for measuring the thermal conductivity of polymers and composites [17]. The rule of mixture model and the series model are the two basic models to measure the thermal conductivity of composites. The rule of mixture retens to CNTs that are arranged in a vertical position in the polymer. This method has high thermal conductivity. While, the series model retens to CNTs that are arranged in the horizontal position. This method has a low level of thermal conductivity. The rule of mixture is predicted by:

$$k_C = k_p \Phi_p + k_m \Phi_m \quad (4.2)$$

where k_C, k_p , and k_m are the thermal conductivity of the composite, particle, and matrix, respectively. Φ_p and Φ_m are volume fraction of particle and matrix, respectively. For the series model the formula is as follows:

$$k_C = 1/\{(\Phi_p/k_p) + (\Phi_m/k_m)\} \quad (4.3)$$

From table 4.2, the results of the sample using 5 vol.% MWNT/LLDPE composites shows a maximum thermal conductivity of 2.59 W/m°C (calculated from the experiment by using Fourier's law in chapter 2 section 2.5.1)

In addition, a method to improve the performance of the solar collector according to Eze [17], and Sivakumar [18], was to make a zig-zag arrangement of water pathways on the collector or a spiral loop of absorbing tube lead to the higher collector efficiency (42% and 53–60%, respectively). It was suggested that, the zig-zag arrangement of the

pathway should be made to improve the performance from 40% to 60% for the solar collector.

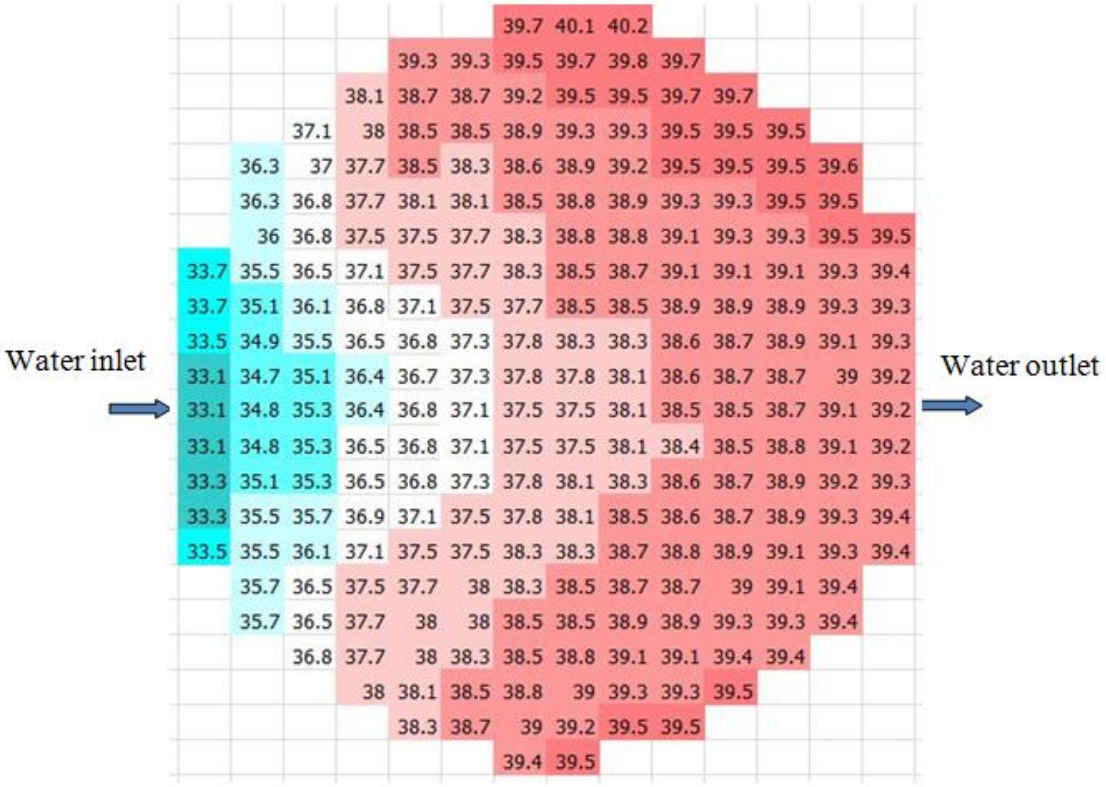

Figure 4.22 Temperature profile of the water as it flowed from the inlet across the surface of the solar heater to the outlet

The temperatures of water were measured as it was flowing from the inlet to the outlet across the absorbing plate, as shown in Figure 4.22. This enabled us to develop a temperature profile of the water heater surface. It is clearly seen that the absorbed heat increased from the inlet to the outlet and also from the center to the edge of the surface due to the longer water pathways. In other words, the longer flowing time on the absorbing plate, the more energy the water gains from the solar collector [17,18]. Therefore, the zig-zag arrangement of MWNT/LLDPE coatings will also improve the solar conversion efficiency of the solar water heating system.

4.8 References

[1] Lemine, O.M., Alyamani, A., Bououdina, M., "Effects of Milling Time on The Formation of Nanocrystalline ZnO," Internatioal Journal Nanotechnology Applied, Vol. 2, No. 1, January 2008, pp. 238–243.

[2] Suntako, R., Laoratanakul, P., Traiphol, N., "Effects of dispersant concentration and pH on properties of lead zirconate titanate aqueous suspension," Ceramics International, Vol. 35, No. 3, April 2009, pp. 1227–1233.

[3] Zeng, R.J. and Rand, B., "Effect of Dispex A40 on Rheology and Filter Pressing Behaviours Concentrated Alumina Suspensions," Journal of Materials Science and Technology, Vol. 17, No. 6, September 2001, pp. 664-666.

[4] Kontopoulou M, Vlachopoulos J., "Melting and Densification of Thermoplastic Powders," Polymer Engineering Science, Vol. 41, No. 5, June 2001, pp. 155-169.

[5] Kontopoulou, M., *Polymer melt formation and densification in rotational molding*, PhD thesis, McMaster University, 1999, pp. 156–159.

[6] Kong, Y. and Hay, J.N., "The measurement of the crystallinity of polymer by DSC," Polymer, Vol. 43, No. 14, June 2002, pp. 3873–3878.

[7] Lee, S., Kim, M.S., Ogale, A.A., "Influence of carbon nanofiber structure on properties of linear low density polyethylene composites," Polymer Engineering Science, Vol. 50, No. 1, January 2010, pp. 93-99.

[8] Kundu, P.P., Biswas, J., Kim, H., et al., "Influence of film preparation procedures on the crystallinity, morphology and mechanical properties of LLDPE films," European Polymer Journal, Vol. 39, No. 8, August 2003, pp. 1585–1593.

[9] Kuan, C.F., Kuan, H.C., Ma, C.C.M., et al., "The preparation of carbon nanotube/linear low density polyethylene composites by a water-crosslinking reaction," Materials Letters, Vol. 61, No. 13, May 2007, pp. 2744-2748.

[10] Ning, Y., "Determination of the crystallinity in different type poly (oxyethylene-styrene) block copolymers by X-ray diffraction method," Chinese Journal Polymer Science, Vol. 7, No. 4, April 1989, pp. 315–321.

[11] Krupa, I. and Luyt, A.S., “Thermal and mechanical properties of LLDPE cross-linked with gamma radiation,” Polymer Degradation and Stability, Vol. 71, No. 3, October 2001, pp. 361–366.

[12] Roro, K.T., Tile, N., Mwakikunga, B., et al., “Solar absorption and thermal emission properties of multiwall carbon nanotube/nickel nanocomposite thin films synthesized by sol-gel process,” Materials Science and Engineering Part B, Vol. 177, No. 8, May 2012, pp.581–587.

[13] Chen, Z. and Bostrom, T., “Electrophoretically deposited carbon nanotube spectrally selective solar absorbers,” Solar Energy Materials and Solar Cell, Vol. 144, No. 1, January 2016, pp. 678-683.

[14] Cheng, B., Wang, K.K., Wang, K.P., et al., “Preparation and characterization of porous carbon- titania nanocomposite films as solar selective absorbers,” J Allo Compou, Vol. 635, No. 25, June 2015, pp. 129-135.

[15] Bera, R.K., Mhaisalkar, S.G., Mandler, D., et al., “Formation and performance of highly absorbing solar thermal coating based on carbon nanotubes and boehmite,” Energy Conversation Managemnt, Vol. 120, No. 15, July 2016, pp. 287–293.

[16] Feng, J., Zhang, S., Liu, X., et al., “Solar selective absorbing coatings TiN/TiSiN/SiN prepared on stainless steel substrates,” Vacuum, Vol. 121, No. 1, November 2015, pp. 135–141.

[17] Eze, J.I. and Ojike, O., “Analysis of thermal efficiency of a passive solar water heater,” International Journal Physical of Science, Vol. 7, No. 22, June 2012, pp. 2891-2896.

[18] Sivakumar, P., Christraj, W., Sridharan, M., et al., “Performance improvement study of solar water heating system,” Journal Engineering and Applied Science, Vol. 7, No. 1, January 2012, pp. 45-49.